



HAL
open science

Precise Mass Measurement of OGLE-2013-BLG-0132/MOA-2013-BLG-148: A Saturn-mass Planet Orbiting an M Dwarf

Natalia Reksini, Virginie Batista, Clément Ranc, David Bennett,
Jean-Philippe Beaulieu, Joshua Blackman, Andrew Cole, Sean Terry, Naoki
Koshimoto, Aparna Bhattacharya, et al.

► **To cite this version:**

Natalia Reksini, Virginie Batista, Clément Ranc, David Bennett, Jean-Philippe Beaulieu, et al..
Precise Mass Measurement of OGLE-2013-BLG-0132/MOA-2013-BLG-148: A Saturn-mass Planet
Orbiting an M Dwarf. *The Astronomical Journal*, 2024, 167 (4), pp.145. 10.3847/1538-3881/ad2514 .
hal-04789839

HAL Id: hal-04789839

<https://hal.science/hal-04789839v1>

Submitted on 20 Nov 2024

HAL is a multi-disciplinary open access archive for the deposit and dissemination of scientific research documents, whether they are published or not. The documents may come from teaching and research institutions in France or abroad, or from public or private research centers.

L'archive ouverte pluridisciplinaire **HAL**, est destinée au dépôt et à la diffusion de documents scientifiques de niveau recherche, publiés ou non, émanant des établissements d'enseignement et de recherche français ou étrangers, des laboratoires publics ou privés.



Distributed under a Creative Commons Attribution 4.0 International License



Precise Mass Measurement of OGLE-2013-BLG-0132/MOA-2013-BLG-148: A Saturn-mass Planet Orbiting an M Dwarf

Natalia E. Reksini^{1,2} , Virginie Batista², Clément Ranc² , David P. Bennett^{3,4}, Jean-Philippe Beaulieu^{1,2} , Joshua W. Blackman^{1,5} , Andrew A. Cole¹ , Sean K. Terry^{3,4,6} , Naoki Koshimoto^{3,4,7} , Aparna Bhattacharya^{3,4}, Aikaterini Vandenrou^{3,4}, Thomas J. Plunkett¹, and Jean-Baptiste Marquette^{2,8}

¹ School of Natural Sciences, University of Tasmania, Private Bag 37 Hobart, Tasmania, 7001, Australia; efstathia.reksini@utas.edu.au

² Sorbonne Université, CNRS, Institut d'Astrophysique de Paris, IAP, F-75014, Paris, France

³ Code 667, NASA Goddard Space Flight Center, Greenbelt, MD 20771, USA

⁴ Department of Astronomy, University of Maryland, College Park, MD 20742, USA

⁵ Physikalisches Institut, University of Bern, Gesellschaftsstrasse 6, 3012 Bern, Switzerland

⁶ Department of Astronomy, University of California Berkeley, Berkeley, CA 94701, USA

⁷ Department of Earth and Space Science, Graduate School of Science, Osaka University, Toyonaka, Osaka 560-0043, Japan

⁸ Laboratoire d'astrophysique de Bordeaux, Univ. Bordeaux, CNRS, B18N, allée Geoffroy Saint-Hilaire, 33615 Pessac, France

Received 2023 November 6; revised 2024 January 17; accepted 2024 January 31; published 2024 March 7

Abstract

We revisit the planetary microlensing event OGLE-2013-BLG-0132/MOA-2013-BLG-148 using Keck adaptive optics imaging in 2013 with NIRC2 and in 2020, 7.4 yr after the event, with OSIRIS. The 2020 observations yield a source and lens separation of 56.91 ± 0.29 mas, which provides us with a precise measurement of the heliocentric proper motion of the event $\mu_{\text{rel, hel}} = 7.695 \pm 0.039$ mas yr⁻¹. We measured the magnitude of the lens in the *K* band as $K_{\text{lens}} = 18.69 \pm 0.04$. Using these constraints, we refit the microlensing light curve and undertake a full reanalysis of the event parameters including the microlensing parallax π_E and the distance to the source D_S . We confirm the results obtained in the initial study by Mróz et al. and improve significantly upon the accuracy of the physical parameters. The system is an M dwarf of $0.495 \pm 0.054 M_{\odot}$ orbited by a cold, Saturn-mass planet of $0.26 \pm 0.028 M_{\text{Jup}}$ at projected separation $r_{\perp} = 3.14 \pm 0.28$ au. This work confirms that the planetary system is at a distance of 3.48 ± 0.36 kpc, which places it in the Galactic disk and not the Galactic bulge.

Unified Astronomy Thesaurus concepts: Gravitational microlensing (672); Adaptive optics (2281); M dwarf stars (982); Exoplanet astronomy (486)

1. Introduction

Gravitational microlensing is a unique method to discover planets down to the mass of Mars around an unbiased sample of stellar types throughout our Galaxy (Gaudi 2012). Its maximum sensitivity is close to the snow line where, according to the core accretion theory, giant planets are mostly formed (Lissauer 1993; Ida & Lin 2004). Furthermore, this method can provide information on cold exoplanet demographics throughout the Milky Way and place constraints on planetary formation scenarios (e.g., Suzuki et al. 2018). Knowledge of the physical parameters of microlensing events can shed light on the regions of very low planetary mass on wide orbits, which are technically difficult to access with other detection methods.

The basic microlensing light curve provides precise measurements of the planet-to-host mass ratio and projected separations in units of the Einstein ring radius. However, additional constraints (e.g., finite-source effects, microlensing parallax) and Bayesian analysis are needed to derive the physical parameters, such as the absolute mass and the semimajor axis of the planetary system. If no microlensing parallax constraint can be used, these physical parameters are often known only to a precision of $\sim 50\%$ or worse. Previous works (Batista et al. 2015; Bennett et al. 2015, 2020;

Ranc et al. 2015; Bhattacharya et al. 2018, 2021; Vandenrou et al. 2020; Blackman et al. 2021; Terry et al. 2021) have shown that adaptive optics (AO) follow-up observations made in the decade following the microlensing event can be used to measure the source–lens flux ratio and separation. This can be translated into a mass–distance relation used to define the physical parameters of the planetary system. Furthermore, when the source and lens are resolved, it is possible to constrain the amplitude and direction of the relative source–lens proper motion. This gives additional constraints that often help to derive masses and projected separation to $\sim 10\%$ precision or better.

In this work we use Keck high angular resolution images, obtained using both NIRC2 and OSIRIS cameras, in order to constrain the planetary mass and distance of OGLE-2013-BLG-0132. Previously Mróz et al. (2017) have shown that this event can be described by a gas giant planet orbiting an M dwarf host star beyond the snow line. M dwarfs are the most abundant type of star in the galaxy (Winters et al. 2015), but the occurrence of gas giant planets orbiting this type of star is very low.

Core accretion theory (Laughlin et al. 2004; Kennedy & Kenyon 2008) predicts that gas giant planets are expected to be rare around low-mass host stars because they form from a runaway process resulting in the rapid accretion of cold gas onto a planetary core (Pollack et al. 1996; Ida & Lin 2004). This means that Jovian and sub-Jovian planet formation requires high solid surface density of the stellar disk and, as a consequence, short timescales. This prediction is borne out in



Original content from this work may be used under the terms of the [Creative Commons Attribution 4.0 licence](https://creativecommons.org/licenses/by/4.0/). Any further distribution of this work must maintain attribution to the author(s) and the title of the work, journal citation and DOI.

Table 1
List of Microlensing Planets Orbiting M Dwarfs, with Mass Measurements Indicating that They Are above Neptune’s Mass

Planet Name	Planet Mass (M_{Jup})	Host Star Mass (M_{\odot})	References
OGLE-2005-BLG-071Lb	3.27 ± 0.32	0.426 ± 0.037	Udalski et al. (2005), Dong et al. (2009), Bennett et al. (2020)
OGLE-2006-BLG-109Lb	0.73 ± 0.06	0.51 ± 0.05	Gaudi et al. (2008), Bennett et al. (2010)
OGLE-2006-BLG-109Lc	0.27 ± 0.02	0.51 ± 0.05	Gaudi et al. (2008), Bennett et al. (2010)
OGLE-2007-BLG-349L(AB)c	0.25 ± 0.04	$0.41 \pm 0.07, 0.30 \pm 0.07$	Bennett et al. (2016)
MOA-2008-BLG-379Lb	3.64 ± 0.51	0.519 ± 0.063	Suzuki et al. (2013), Bennett et al. (2023)
MOA-2009-BLG-319Lb	0.212 ± 0.20	0.524 ± 0.048	Miyake et al. (2011), Terry et al. (2021)
OGLE-2003-BLG-235Lb	2.34 ± 0.43	0.56 ± 0.06	Bond et al. (2004), Bhattacharya et al. (2023)
MOA-2010-BLG-117Lb	0.54 ± 0.10	0.58 ± 0.11	Bennett et al. (2018)
OGLE-2012-BLG-0950Lb	0.123 ± 0.025	0.58 ± 0.04	Koshimoto et al. (2016), Bhattacharya et al. (2018)
OGLE-2013-BLG-0132Lb	0.260 ± 0.028	0.495 ± 0.054	Mróz et al. (2017)

planetary population synthesis models treating the host star, disk, and planetesimal accretion self-consistently in N -body simulations (e.g., Burn et al. 2021), where the gas giant frequency diminishes with decreasing stellar mass and is expected to be very low for $M_* \lesssim 0.5 M_{\odot}$. Considering a realistic disk-to-star mass ratio for M dwarfs would imply that the disks around this type of star are expected to have difficulty exceeding the threshold density for giant planet formation (Burn et al. 2021).

Furthermore, the core accretion disk theory predicts a desert area for planets with M_p from 10 to $100 M_{\oplus}$ for orbital distances less than 3 au. OGLE-2013-BLG-0132 falls into this intermediate stage with a planet mass of $82.6 M_{\oplus}$ and projected separation of 3.14 ± 0.28 au. The discovery of Jovian and sub-Jovian planets orbiting M dwarf stars beyond the snow line could imply that the distribution of giant planets is similar for host stars of $0.5 M_{\odot}$ and those of $1.0 M_{\odot}$ but the number of giant planets is larger for larger host star masses.

Until today there have been nine confirmed microlensing cases of giant planets orbiting host stars with masses $\lesssim 0.6 M_{\odot}$ that can support this idea. The list of these planets and of the papers confirming their mass measurements is presented in Table 1. All of the masses of these planets have been determined by our Keck follow-up observations (fourth column). From the confirmed detections presented here, OGLE-2006-BLG-109Lc and MOA-2009-BLG-319Lb have similar planet and host star masses to OGLE-2013-BLG-0132, while OGLE-2005-BLG-071Lb and OGLE-2003-BLG-235Lb represent super-Jupiter planets orbiting M dwarfs.

Here we combine the microlensing light-curve model and the constraints from adaptive optics to acquire a precise mass measurement of the planet–host star system and confirm the event to be in the list of gas giant exoplanets with M dwarf host stars. Finally, we discuss the significance of the dependence on host star mass for the exoplanet formation models.

This paper is organized as follows. First, in Section 2 we discuss the discovery and previous work on OGLE-2013-BLG-0132Lb. In Section 3 we describe our Keck AO high angular resolution images and the methods used for image calibration and photometry. We then detail our measurements of lens–source relative proper motion and flux ratio. In Section 4 we perform a Markov Chain Monte Carlo fit to the updated light-curve data of the event using the AO constraints and present the best-fit model. In Section 5 we present the physical parameters of the planetary system. Finally, we discuss our results and conclude the paper in Section 6.

2. The Microlensing Event OGLE-2013-BLG-0132

OGLE-2013-BLG-0132 was discovered and announced by the Optical Gravitational Lensing Experiment (OGLE) Early Warning System (Udalski et al. 1994, 2004) on 2013 March 3. It was also discovered independently as MOA-2013-BLG-148 by the Microlensing Observations in Astrophysics (MOA) collaboration (Bond et al. 2001). The equatorial coordinates of the event are R.A. = $17^{\text{h}}59^{\text{m}}03^{\text{s}}.51$, decl. = $-28^{\circ}25'15''.7$ (J2000.0) and the Galactic coordinates are $l = 1^{\circ}944$, $b = -2^{\circ}275$.

The analysis of the event by Mróz et al. (2017) yields a Saturn-mass planet orbiting an M dwarf. Due to the faintness of the source and the short timescale of the event, they obtained only an upper limit on the parallax magnitude $\pi_E \leq 1.4$. They derive the angular Einstein radius $\theta_E = 0.81 \pm 0.12$ mas and the Einstein time $t_E = 36.99 \pm 0.77$ days. This led to a fairly high proper motion of $\mu_{\text{rel, hel}} = 8.0 \pm 1.3$ mas yr $^{-1}$. This value implies a 60 mas source–lens separation after 7.5 yr, comparable to the expected FWHM, in the best conditions, with Keck AO systems. This makes OGLE-2013-BLG-0132 a very good candidate for follow up with high angular resolution imaging.

In Mróz et al. (2017) the light-curve model gives a planet–star mass ratio of $q = (5.15 \pm 0.28) \times 10^{-4}$. Using a Bayesian analysis and assuming that host stars of all masses are equally likely to host a planet of this mass ratio, they estimate the masses of planet and host star respectively to be $m_p = 0.29^{+0.16}_{-0.13} M_{\text{Jup}}$ and $M = 0.54^{+0.30}_{-0.23} M_{\odot}$, making the host star an M dwarf. They performed a grid search on three microlensing parameters (q, s, α), where q is the planet–star mass ratio, s is the projected separation, and α is the angle of the source trajectory with respect to the lens axis. The source angular radius is considered fixed, using a sequential least-squares algorithm (Kraft 1985). The source flux magnification was calculated using the ray-shooting method (Schneider & Weiss 1986), considering the point-source approximation far from the caustic crossings and the hexadecapole approximation at intermediate distances (Gould 2008).

In Mróz et al. (2017) the estimated brightness of the source at baseline is $I_S = 19.37 \pm 0.03$ and the color $(V - I)_S = 1.79 \pm 0.04$. They also measured the red clump centroid on a color–magnitude diagram, giving $I_{\text{RC}} = 15.62$ and $(V - I)_{\text{RC}} = 2.07$. Assuming that the source is affected by the same amount of extinction as the red clump stars from the field (Bensby et al. 2011; Nataf et al. 2013), they derived the dereddened color and brightness of the source star: $(V - I)_{S,0} = 0.78 \pm 0.04$ and $I_{S,0} = 18.11 \pm 0.20$.

Our KECK AO observations are in the K band so we need to transform the I_S magnitude into K magnitude in order to compare our AO results with the fitting model. We choose to use the method of Surot et al. (2020) for calculating the $(J - K_S)$ extinction for the (l, b) Galactic coordinates of the event. Surot et al. (2020) provide a direct high-resolution ($2'$ to $\sim 10''$) color excess map for the VISTA Variables in the Vía Láctea (VVV) bulge area in $(J - K_S)$ color, so by using their method we reduce the possible error propagation caused by color-color relations (Bessell & Brett 1988). We find $E(J - K_S) = 0.336 \pm 0.015$ for $(l, b) = (1^\circ 944, -2^\circ 275)$. We define the A_K extinction along the line of sight as the total extinction up to the Galactic Center. We use the dereddened red clump magnitudes of Nishiyama et al. (2009) and obtain $A_J/A_K = 3.02$, which leads to $E(J - K_S) = 2.02A_K$ and finally $A_K = 0.181 \pm 0.007$.

Finally, we predict the source magnitude in the K band to be

$$K_{\text{source}} = V_{S,0} - (V - K)_{S,0} + A_K = 17.35 \pm 0.20. \quad (1)$$

As we show in Section 3.4, our AO observations in the K band confirm this source magnitude. Summaries of the color and extinction values are given in Tables 5 and 2 respectively.

3. High-resolution Imaging Follow-up

3.1. Analysis of the 2013 NIRC2 Images

We obtained JHK observations of the target OGLE-2013-BLG-0132 with the NIRC2 instrument and the wide camera (covering a field of $40''$) on Keck II in 2013 July, five months after the peak of the microlensing event. The K -band images had a point-spread function (PSF) FWHM of 90 mas. These observations are used to obtain a calibrated flux measurement at the position of the source, since source and lens are not expected to be resolved that early after the microlensing event. We dark-subtracted and flat-fielded the images following standard procedures, and we stacked the images using SWARP (Bertin 2010). We then used the GAIA catalog to refine the astrometry of the stacked frames. Finally, using TOPCAT (Shopbell et al. 2005), we cross-identified the catalogs of our reanalysis of the VISTA 4 m telescope VVV survey (Minniti et al. 2010) with the KECK sources measured with the SExtractor program (Bertin & Arnouts 1996). The procedures are described in detail in Beaulieu et al. (2016, 2018).

In the $40''$ NIRC2 field of view we cross-identified 70 stars also measured in the VVV catalogs. We then calibrate the KECK frame and estimate that we have an error of the zero-point at 2.0% (systematics). We finally provide our measurement of calibrated magnitudes of the source+blended light:

$$\begin{aligned} J_{2013} &= 17.85 \pm 0.05 \\ H_{2013} &= 17.22 \pm 0.04 \\ K_{2013} &= 17.05 \pm 0.04. \end{aligned} \quad (2)$$

3.2. Analysis of the 2020 OSIRIS Images

The second set of observations for the target took place on 2020 August 17 and 18 using the OSIRIS imager on Keck I. These data were taken using the K_p filter and had an average FWHM of 56 mas. The pixel scale of the OSIRIS camera is $9.96 \text{ mas pixel}^{-1}$.

We have obtained 25 K_p science images with an individual exposure time of 60 s, with five dithered positions with an amplitude of $1''$, 80 flat-field frames, 30 dark, and 10 sky

Table 2
Adopted Extinction and Reddening Values to the Source

Parameter	Value
A_J	1.26 ± 0.012
A_K	0.181 ± 0.007
$E(J - K_S)$	0.336 ± 0.015

frames (60 s). We used the Keck AO Imaging (KAI) data reduction pipeline (Lu et al. 2021) to correct dark current, flat-fielding, instrumental aberrations of the OSIRIS camera, and the sky. This tool performs corrections to the 25 science images using the dark, flat-field, and sky frames and stacks them into a single master science frame. We then perform the astrometry calibration using the GAIA catalog as performed for the 2013 NIRC2 images. The combined science frame is presented in Figure 1. In order to obtain precise positions of the source and lens in the 2020 observations we need to construct an empirical PSF fit for each star individually. We use the methods shown in Bhattacharya et al. (2018, 2021), starting with the PSF fitting routine of the DAOPHOT-II package (Stetson 1987). Once we generate an empirical PSF model we fit it to both source and lens. To do that we fit a two-star PSF to the target using DAOPHOT. The residuals from this method are shown on the right side of Figure 1.

We now have a first guess about the pixel positions of source and lens and their empirical magnitudes, but DAOPHOT does not produce a probability distribution of all possible solutions for our target. It also does not report error bars for the positions of the two stars, which means that we cannot calculate the precision of the source-lens relative proper motion. For this reason we use a modified version of the original DAOPHOT package (Terry et al. 2021), which contains a supplementary routine that uses the Markov Chain Monte Carlo (MCMC) method to produce a probability distribution for the source-lens parameter space. This parameter space contains six parameters: the x, y pixel positions of source and lens, the total flux, and the total flux ratio of the two stars. Finally, the routine calculates χ^2 of each possible solution and returns as a best-fit solution the parameter set with the minimum χ^2 value.

The quality of AO images is affected by the Strehl ratio. Variability in the atmospheric conditions during observations means that the Strehl ratio and the PSF FWHM values will vary from image to image. Therefore, a single master science frame may contain significant imperfections, due to one or more images, that will be included in our PSF model and MCMC results. For this reason we use the jackknife routine (Tukey 1958) implemented in the KAI_Jackknife data reduction pipeline as described in Bhattacharya et al. (2021). Using this package, we analyze a collection of $N = 25$ science images and produce N images of $N - 1$ stacked science images. This method helps us detect possible problematic frames and also offers error bars that include the uncertainties of the PSF variations. Finally, we perform the *DAOPHOT_MCMC* routine analysis in all 25 jackknife frames. We do that using the same reference stars and magnitude of the target for each frame. We obtain best-fit values and errors from each MCMC routine and calculate the Jackknife error. Our final uncertainties are the jackknife and MCMC errors added in quadrature, as presented in Table 4.

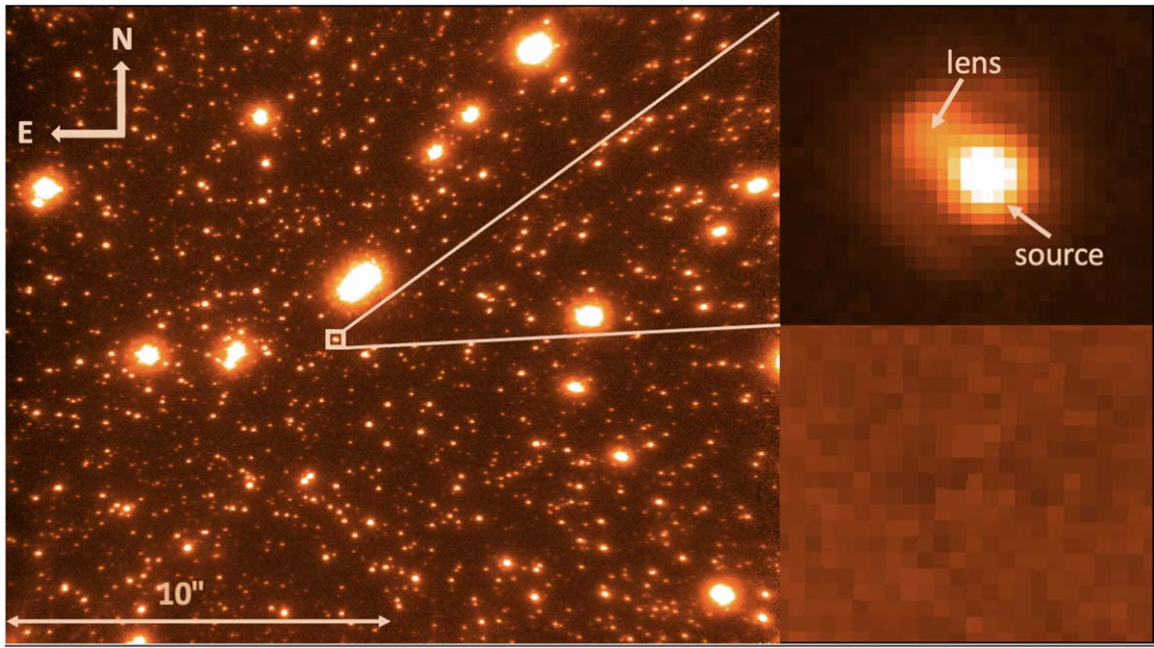


Figure 1. Left panel: jackknife stack of 24 (60 s) frames of the 2020 Keck OSIRIS K_p band follow-up observation. Upper right panel: close-up ($2''.5 \times 2''.5$) frame of the source and lens. Lower right panel: close-up ($2''.5 \times 2''.5$) of the two-star PSF fit residual using DAOPHOT.

Table 3
DAOPHOT Results for the Two-star and Three-star PSF Fits for the 2020 OSIRIS Images

Model	Component	Coordinates	Mag.	s (mas)	F	χ^2/dof
Two-star model	Star1	[1210.92, 1420.87]	12.867
	Star2	[1206.48, 1424.46]	14.261
	56.885	0.7806	544.12/621
Three-star model	Star1	[1210.93, 1420.88]	12.729
	Star2	[1206.48, 1424.47]	14.146
	Star3	[1211.48, 1405.44]	17.269
...	56.798	0.7781	259.42/618

Note. The pixel coordinates, instrumental magnitude, separation, total flux ratio, and χ^2 values for the two-star and three-star PSF fitting models. The values show the results of the basic DAOPHOT routine for only one image combination of $N - 1$ image frames. The differences in separation and total flux ratio between the two models are inside the value's uncertainties derived by Mróz et al. (2017).

3.3. Resolving Source and Lens

Mróz et al. (2017) gave a source–lens heliocentric relative proper motion of $\mu_{\text{rel}} = 8.0 \pm 1.3 \text{ mas yr}^{-1}$. We therefore expected a source and lens separation of ~ 60 mas in 2020, which is comparable to the average PSF FWHM of the OSIRIS images.

A visual inspection of the KAI_Jackknife combined images showed two stars at the position of the microlensing event (Figure 1). Thus, source and lens are resolved enough for the DAOPHOT routine to be able to identify them as two separate stars. Due to the crowded image the routine identifies a nearby third star at a distance of 16 pixels from the source–lens center. We compare the parameter space results for two-star and three-star PSF fits using the basic DAOPHOT routine. In Table 3 we present the results of our DAOPHOT analysis for the two-star and three-star PSF models including the pixel coordinates and instrumental magnitudes for each star component. We measure the separation and the total flux ratio $F = F1/(F1 + F2)$ between star1 and star2 for each model case. Our three-component frame and the three-star residual are shown in Figure 2. We find the third component to have a separation of

~ 154 mas from the first star and ~ 196 mas from the second star. Furthermore it has a magnitude difference of more than five magnitudes from the bright star (star1) and almost 3 mag from the faint star (star2). Its large separation from the other components and its faintness make it an unsuitable candidate for either the source or the lens in this study. In addition, the difference in the source–lens separation between the two-star and three-star models is 0.565 mas, thus the difference between the two models is less than the error in relative proper motion derived from Mróz et al. (2017). Since our results for the source–lens separation and flux ratio are not significantly affected by the inclusion of the third star in the group we decided to maintain the two-star model for the rest of this work. We present our final results for the source–lens separation, relative proper motion and flux ratio in Table 4.

3.4. Flux Ratio

We start by measuring the magnitude in the K_p band for the source and lens separately. As shown in Section 3.1 the source–lens blending magnitude measured by the KECK 2013 images is $K_{\text{Keck}} = 17.05 \pm 0.04$. The DAOPHOT_MCMC analysis of

Table 4
DAOPHOT_MCMC and Jackknife Best-fit Results for the 2020 Osiris Images

Parameter	Median	MCMC rms	Jackknife rms	MCMC + JK rms
Separation (mas)	56.911	± 0.232	± 0.174	± 0.290
$\mu_{\text{rel,HE}}$ (mas yr ⁻¹)	-4.824	± 0.026	± 0.029	± 0.039
$\mu_{\text{rel,HN}}$ (mas yr ⁻¹)	5.985	± 0.029	± 0.032	± 0.043
$\mu_{\text{rel,helio}}$ (mas yr ⁻¹)	7.695	± 0.031	± 0.024	± 0.039
$\mu_{\text{rel,geo}}$ (mas yr ⁻¹)	7.594	± 0.034	± 0.040	± 0.052
Flux ratio	0.2848	± 0.0028	± 0.0019	± 0.003

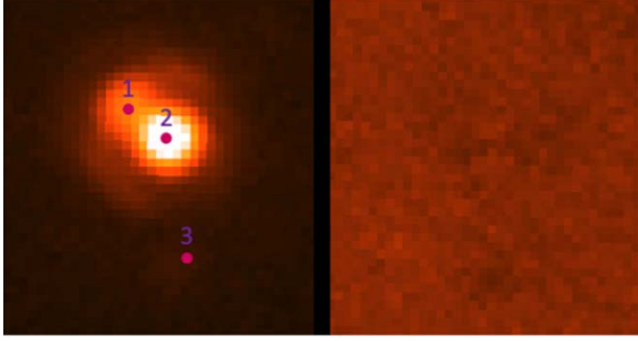


Figure 2. Left panel: close-up frame (400×420 mas) of the three-star group selection by DAOPHOT. Right panel: residual of the three-star PSF fit.

the 2020 OSIRIS images yields the total flux ratio for the two stars to be $F = 0.778 \pm 0.001$. By combining the previous results with the equations for absolute magnitude and flux ratio, we calculate the source and lens absolute magnitudes:

$$\frac{f_L}{f_S} = \frac{1 - F}{F}, \quad (3)$$

$$K_{\text{Keck},L} - K_{\text{Keck},S} = -2.5 \log_{10} \left(\frac{f_L}{f_S} \right) \quad (4)$$

and

$$K_{\text{Keck}} = -2.5 \log_{10} (10^{-0.4K_{\text{Keck},S}} + 10^{-0.4K_{\text{Keck},L}}). \quad (5)$$

The results we obtain from these Keck observations and from the light-curve best-fit model imply that the brightest star corresponds to the source. In addition, in Table 5 we compare our magnitude of the brightest star with the magnitude of the source star deduced by Mróz et al. (2017) and show that the two magnitudes are in good agreement. This is a strong proof of the identification of the source star, and as a result we have

$$\begin{aligned} f_L/f_S &= 0.2848 \pm 0.0019 \\ K_{\text{Keck},L} &= 18.69 \pm 0.04 \\ K_{\text{Keck},S} &= 17.32 \pm 0.04. \end{aligned}$$

3.5. Lens–Source Relative Proper Motion

There exist two methods for measuring the source–lens relative proper motion. One method would be to use the finite-source effects on the light curve, if these are detected, and a color–magnitude diagram (Boyajian et al. 2014). Dividing the angular source radius θ_* by the crossing time for the source radius t_* leads to the measurement of the geocentric relative proper motion $\mu_{\text{rel,geo}} = \theta_*/t_*$. Using the values from the light-curve fitting model presented in Section 4, we find that

Table 5
Source Flux Values

Parameter	Mroz et al. (2017)	This Work
$I_{S,0}$	18.11 ± 0.20	18.01 ± 0.04
$K_{S,0}$	17.365 ± 0.20	17.32 ± 0.04

$\mu_{\text{rel,geo}} = 7.684 \pm 0.881$ mas yr⁻¹. This measurement of the relative proper motion yields an angular Einstein radius of $\theta_E = 0.78 \pm 0.09$ mas.

Another way to deduce the relative proper motion and then the angular Einstein radius, with higher precision, is the use of AO follow-up images. Here the 2020 Osiris images give us a separation $s = 56.911 \pm 0.290$ mas, 7.403 yr after the peak of the microlensing event. We convert it into a heliocentric relative proper motion $\mu_{\text{rel,hel}} = 7.688 \pm 0.039$ mas yr⁻¹. In Table 4 we present our final results from the 2020 Osiris images.

Since the light-curve model uses a geocentric reference frame, relative proper motion must be expressed in the inertial geocentric frame. We use the relation given by Dong et al. (2009) in order to convert the heliocentric relative proper motion into geocentric relative proper motion $\mu_{\text{rel,geo}}$:

$$\mu_{\text{rel,geo}} = \mu_{\text{rel,helio}} - \Delta\mu \quad (6)$$

where

$$\Delta\mu = \frac{\pi_{\text{rel}} V_{\oplus,\perp}}{\text{au}} = \left(\frac{1}{D_L} - \frac{1}{D_S} \right) V_{\oplus,\perp}. \quad (7)$$

$V_{\oplus,\perp}$ represents the velocity of the Earth projected on the sky at the R.A., decl. coordinates at the peak of the microlensing event ($17^{\text{h}}59^{\text{m}}03^{\text{s}}.689$, $-28^{\circ}25'16''29$). The velocity is expressed in north and east coordinates:

$$V_{\oplus,\perp} = (2.61, -1.45) \text{ km s}^{-1}. \quad (8)$$

Calculation of the relative distance of the source–lens from π_{rel} demands the definition of the distance of the lens at the time of the event. In Section 5 we use the high angular resolution data to constrain the light-curve fitting models that provide microlensing parallax values that are in agreement with the AO results for the source–lens relative proper motion and the flux of the lens. This method leads to $\pi_{\text{rel}} = 0.423 \pm 0.030$ kpc⁻¹, which yields a geocentric relative proper motion of 7.594 ± 0.052 mas yr⁻¹. Finally, using this method we deduce an angular Einstein radius of $\theta_E = 0.785 \pm 0.017$ mas.

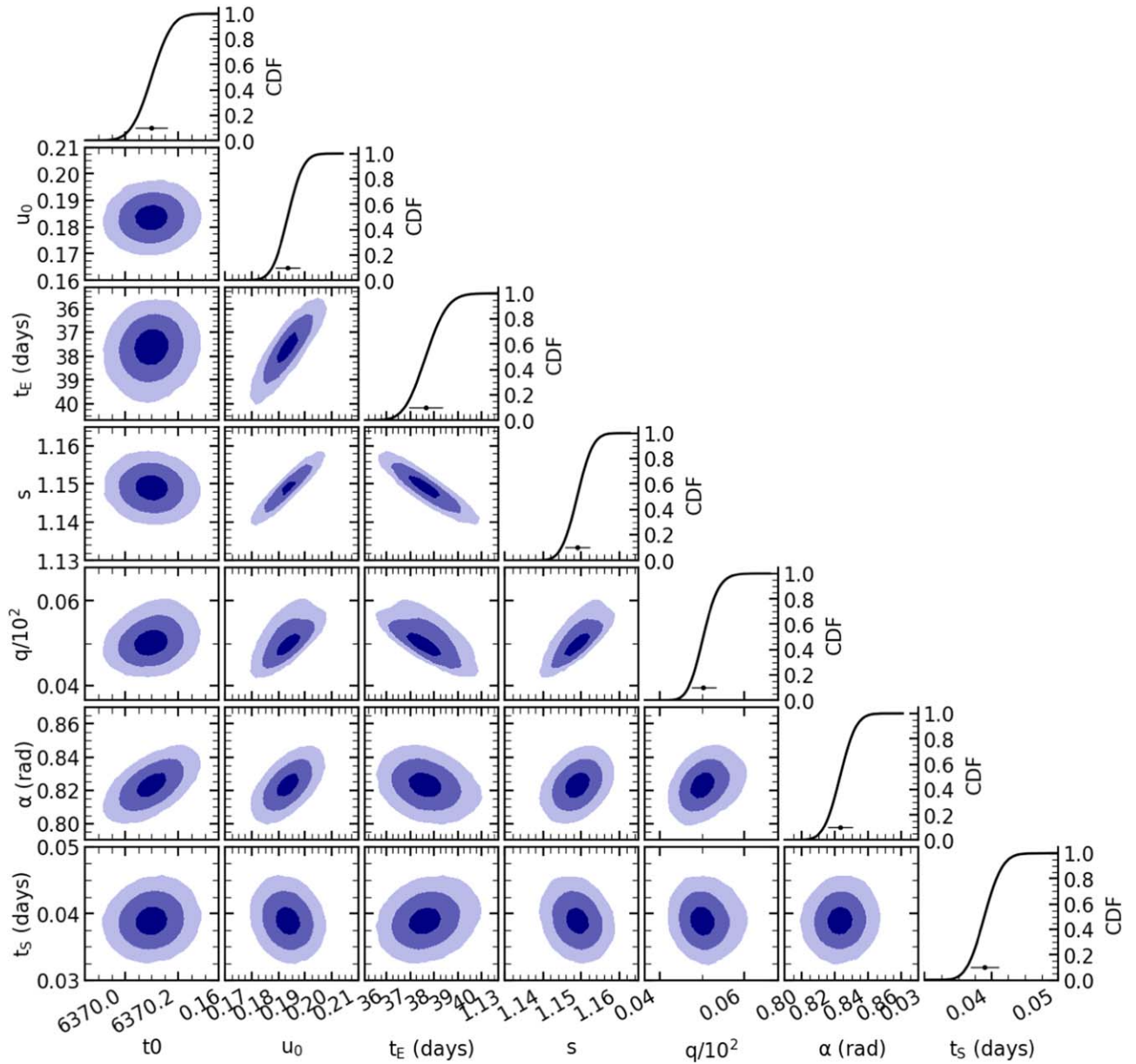


Figure 3. The marginalized posterior distributions of the light-curve best-fit model. On the diagonal we show the one-dimensional cumulative density function of each parameter. The 68.3% (1σ), 95.5% (2σ), and 99.7% (3σ) confidence intervals are represented by dark, median, and light violet respectively.

4. Light-curve Fitting

In this work we use a modified version of the imaged-centered ray-shooting light-curve modeling code of Bennett & Rhie (1996) and Bennett (2010), which now goes by the name `eesunhong`⁹, in honor of the original coauthor of the code (Bennett & Khavinson 2014; Bennett 2014). This new version of the `eesunhong` code incorporates constraints from Keck AO on lens flux measurements and lens–source relative proper motion on the light-curve models. This code also includes the microlensing parallax parameters, even when they are not determined by the light curve, because they are tightly constrained by the relative proper motion measurements and the lens magnitude. Inclusion of the microlensing parallax can be important because the microlensing parallax parameters can

influence the crossing time of the Einstein radius and the inferred magnitude of the source star, as was shown by Bennett et al. (2023).

There is a complication that comes from using the measured relative proper motion from the Keck AO data to constrain the microlensing parallax, because the Keck AO data determine the relative proper motion in the Heliocentric reference frame, $\mu_{\text{rel,helio}}$, while the microlensing parallax vector is parallel to the relative proper motion, $\mu_{\text{rel,geo}}$, in the inertial geocentric frame that moves with the Earth at the time of the event. This requires that we add the source distance, D_s , as a model parameter, which we constrain with a prior from a Galactic model (Koshimoto et al. 2021).

This modeling method is explained in more detail in Bennett et al. (2023), and has also been used in the analysis of OGLE-2016-BLG-1195 (Vandorou et al. 2023).

⁹ <https://github.com/golmschenk/eesunhong>

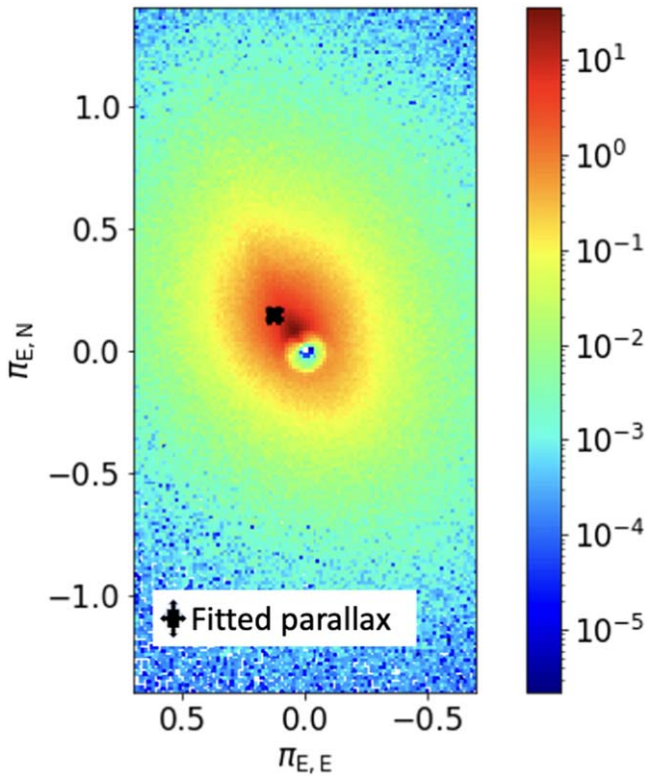


Figure 4. Two-dimensional parallax distribution based on the Galactic model (*genulens*). The color scale shows the relative probability; the black cross indicates the microlensing parallax predicted using our (AO) Keck constraints.

4.1. Survey Data

The event OGLE-2013-BLG-0132 was only observed by the OGLE and MOA ground-based photometric surveys (Mróz et al. 2017). The MOA photometric data contained systematic errors due to the faintness of the source star, weather conditions, and also the larger pixel scale than OGLE. For this reason Mróz et al. (2017) used only a subset of the MOA data set within ± 10 days of the peak, including the caustics and ignoring the wings. Here we revisit the modeling of the light curve using a re-reduction of MOA data, which performs a detrending process to correct for systematic errors and removes correlations in the data (Bond et al. 2017). We were therefore able to use three years of data around the peak of the event. Finally, Mróz et al. (2017) mentioned a long-term trend in the OGLE data, which was treated before their light-curve fitting. This trend is probably caused by a very bright nearby star that is moving with respect to the target. Since no microlensing parallax had been observed, the OGLE data treatment is sufficient for modeling this event.

4.2. Light-curve Modeling

The model presented by Mróz et al. (2017) shows no ambiguity in the light-curve parameters and we have no reason to expect significant differences using the re-reduced data. Eeshunhong uses high angular resolution results for the source–lens relative proper motion and the flux of the lens as additional constraints in the MCMC analysis. This method ensures that the light-curve parameters are consistent with the AO follow-up observations and allows us to fit the microlensing parallax, even when this hasn’t been observed/constrained during the event. We modeled the light curve of the event using the

Table 6
Light-curve Best-fit Model Parameters

Parameter (1)	MCMC (lc) (2)	MCMC (lc + AO) (3)	Mroz et al. (2017) (4)
t_E (days)	37.60 ± 0.72	37.40 ± 0.26	36.99 ± 0.77
t_0 (HJD $^{\circ}$)	6370.097 ± 0.059	6370.062 ± 0.059	6370 ± 0.064
u_0	0.183 ± 0.004	0.185 ± 0.001	0.184 ± 0.005
s	1.149 ± 0.003	1.1502 ± 0.0009	1.150 ± 0.004
α (rad)	0.822 ± 0.005	0.821 ± 0.006	0.821 ± 0.008
$q \times 10^{-4}$	5.00 ± 0.27	5.00 ± 0.28	5.15 ± 0.28
t_* (days)	0.038 ± 0.002	0.0387 ± 0.0016	0.037 ± 0.004
I_s	19.349 ± 0.031	19.277 ± 0.004	19.37 ± 0.03
$\pi_{E,E}$...	0.129 ± 0.019	...
$\pi_{E,N}$...	0.145 ± 0.023	...
π_E	...	0.195 ± 0.023	< 1.4
D_s (kpc)	...	7.405 ± 0.710	...
χ^2	9389/9404	9384/9401	1104/1019

Note. We show the MCMC mean values and 1σ results for the best fit obtained using only the light-curve data (Column (2)), the light-curve data and the constraints derived by our 2020 Keck follow-up images (Column (3)) and the results presented by Mróz et al. (2017) in the discovery paper (Column (4)).

image-centered ray-shooting method (Bennett & Rhie 1996). We begin by using the original light-curve fitting code and exploring the parameter space for a binary lens and a single source star (2L1S), using the best-fit results presented in Mróz et al. (2017) as initial conditions.

There are seven basic parameters that describe the shape of a light curve of a microlensing event. Three of these parameters describe both a single and a binary lens model: t_E , the crossing time of the Einstein radius that defines the event’s timescale, t_0 , the time of the minimum approach of the center of mass of the lens, and u_0 , the impact parameter relative to this center of mass. When the source star transits a caustic or a cusp, we can measure the fourth parameter t_* , the crossing time of the source radius. We use finite-source effects for the measurement of the source–lens relative proper motion.

The final three parameters describe the physical parameters of a binary lens system. These are the mass ratio, q , of the planet and star, their projected separation, s , in Einstein radius units, and the angle between the planet–star separation vector and the source trajectory, α . We fit the light-curve model by using this set of parameters in order to predict the flux of the event. To do this we fit two additional observational parameters per observing site: the source star flux F_s , and the unmagnified blend flux F_b , which might include the lens flux as well as close neighbor stars. The light-curve model is defined as $F(t) = A(t)F_s + F_b$, where $F(t)$ is the flux of the event at time t .

Once we fit the light curve we used an MCMC algorithm with a Metropolis Hastings sampler to inspect the posterior distributions of the lens physical parameters as shown in Figure 3. We then use the mean values of the distributions as initial conditions for our second light-curve fitting, which contains the source–lens relative proper motion and the lens magnitude found as a prior in Section 3.3 from the Keck 2020 follow-up images. These two parameters, when defined with high accuracy, place a strong constraint on the microlensing parallax. We show that the model describes the planetary anomaly with high precision. In Figure 4 we show the two-dimensional parallax values that the best-fit model yields plotted on the parallax distribution based on the Bayesian analysis (*genulens*) described in Koshimoto et al. (2021) and

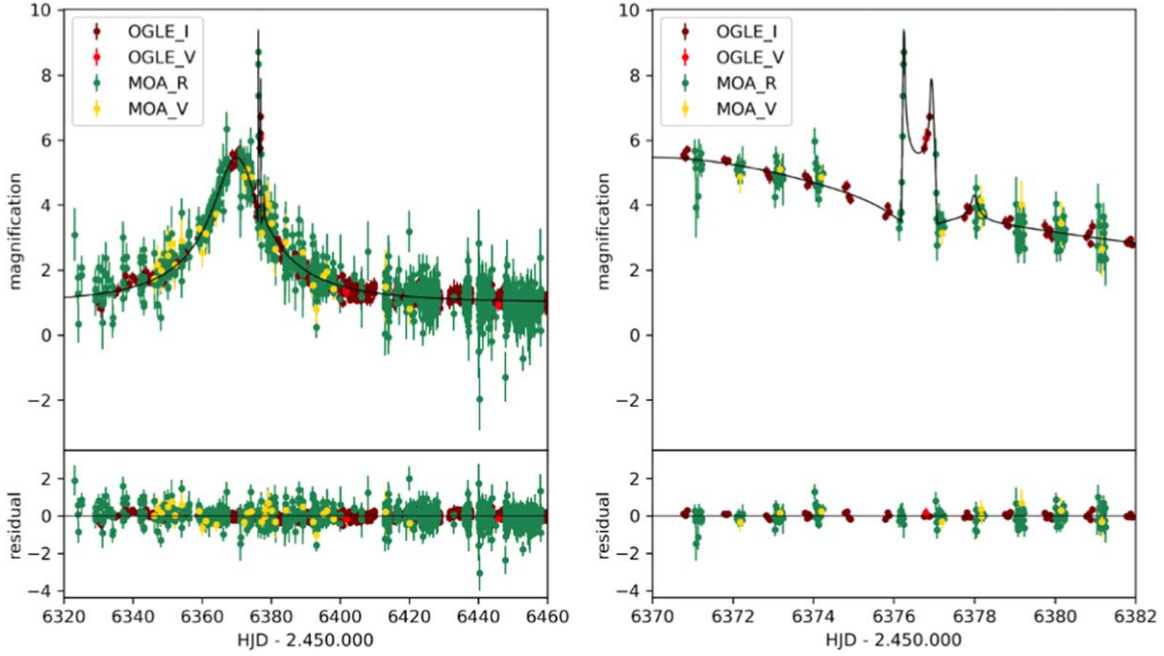


Figure 5. Light curve of OGLE-2013-BLG-0132. The right panel shows the enlargement of the caustic-crossing part of the light curve. The best-fit model is indicated by the black curve. The bottom panel shows the residual from the best-fit model and the OGLE and MOA data. The figures were made using the software described in Ranc (2020).

Koshimoto & Ranc (2022). The parallax deduced by the Keck constraints matches the region of high relative probability predicted by the Galactic model. As mentioned in Section 3.5 the relative proper motion must be in geocentric coordinates for defining θ_e . This means that we need to include the distance to the source as a fitting parameter in our light-curve model. For the initial estimate we choose to use the D_s value calculated by the Koshimoto et al. (2021) Galactic model. Fitting a parallax distribution that is in agreement with the high angular resolution follow up leads to an additional constraint for the mass and distance of the planetary system. Figure 5 shows the light-curve best fit and the residual from the MOA and OGLE data during the magnification event. We show that the model describes the planetary anomaly with high precision.

Our fitting parameters are consistent with the Mróz et al. (2017) results with some small differences in the crossing time of the Einstein radius, the mass ratio, and the modeled source flux. We have achieved a significant increase in the accuracy in most of our parameters upon the previously published results, especially for u_0 , s , t_* , and I_s . We present all the parameters in Table 6.

We remeasured the calibrated source color to $(V - I)_S = 1.79 \pm 0.04$ and deduce the dereddened color and I -band magnitude of the source star as $(V - I)_{S,0} = 0.78 \pm 0.04$ and $I_{S,0} = 18.01 \pm 0.04$. Finally, we use the dereddened values of the source star in combination with the surface brightness relations from Boyajian et al. (2014) in order to determine the angular source size θ_* :

$$\log(2\theta_*) = 0.5014 + 0.419(V - I)_{S,0} - 0.2I_{S,0}, \quad (9)$$

which gives us an angular source size of $\theta_* = 0.80 \pm 0.08 \mu\text{as}$.

This result is in good agreement with Mróz et al. (2017) but with improved error bars.

5. Planetary System Parameters

The lens magnitude and lens–source separation we have deduced from our (AO) images permit us to use all three empirical mass–luminosity relations and finally derive a measurement of the mass and distance of the lens.

First, we use a mass–distance relation from resolving the source and lens system ($\mu_{\text{rel,geo}}$), which constrains the angular Einstein ring radius (θ_E) as shown in Section 3.5:

$$M_L = \frac{\theta_E^2}{\kappa \pi_{\text{rel}}}, \quad (10)$$

with $\pi_{\text{rel}} = (D_L^{-1} - D_S^{-1})$ au the relative source and lens distance and $\kappa = 4G/c^2$ au = 8.144 mas M_\odot^{-1} . M_L is the lens mass, D_L the distance to the lens, and D_S the distance to the source derived from the light-curve best fit in Section 4.

For the second mass–distance relation we use the microlensing parallax expressed by

$$\pi_E = \sqrt{\frac{\pi_{\text{rel}}}{\kappa M_L}}. \quad (11)$$

Finally, we proceed by correlating the lens magnitude measured by Keck with a calibrated population of main-sequence stars. For this we use isochrones (Girardi et al. 2002) that provide a mass–luminosity function for different ages and metallicities of main-sequence stars. We decide to use isochrones for ages 500 Myr to 6.4 Gyr and metallicities within the range $0.0 \leq [\text{Fe}/\text{H}] \leq +0.2$. We finally combine the lens magnitude and the isochrones in order to deduce an independent mass–distance relation:

$$m_L(\lambda) = 10 + 5 \log_{10}(D_L/1 \text{ kpc}) + A_{K_L}(\lambda) + M_{\text{isochrone}}(\lambda, M_L, \text{age}, [\text{Fe}/\text{H}]), \quad (12)$$

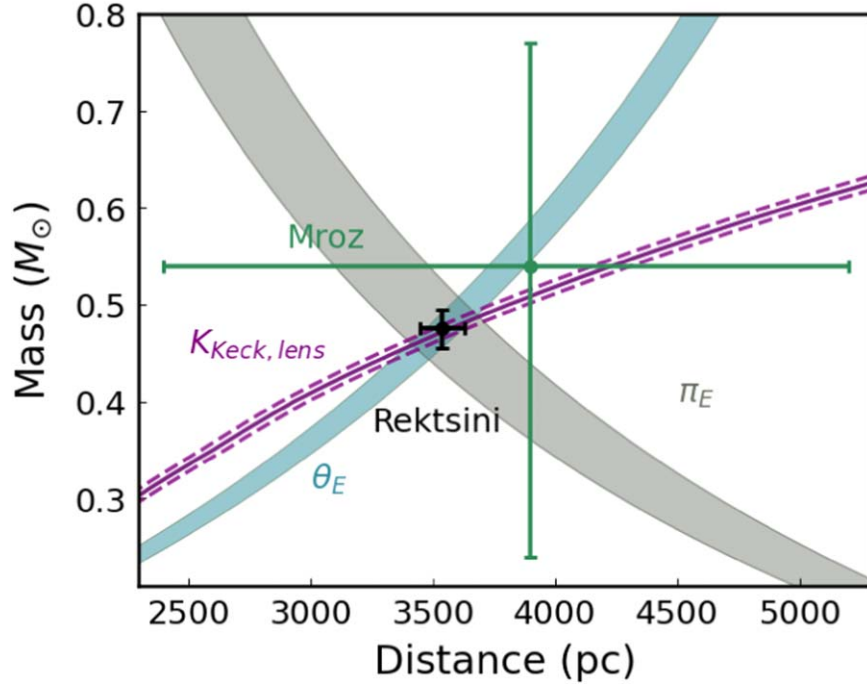


Figure 6. Mass–distance estimate for the lens. The purple curve represents the constraint from the K -band measurement of lens flux, the sea green curve shows the measurement of Einstein angular radius, and the gray curve represents the microlensing parallax calculated using the (AO) constraints. The intersection between the three curves defines the estimated solution of the lens physical parameters.

where m_L is the magnitude of the lens, A_{K_L} is the extinction to the lens, here in the K band, and $M_{\text{isochrone}}$ is the absolute magnitude of the lens star at wavelength λ . We can determine the distance and the mass of the lens through the intersection of these three relations as shown in Figure 6.

A_{K_L} is estimated by considering the source distance and reddening determined above and the distribution of Galactic dust relative to the source and lens distances. We calculate it as a function of the lens distance D_L , given its Galactic coordinates $(l, b) = (1^\circ 9444, -2^\circ 2745)$. Assuming that the dust in the Milky Way is distributed exponentially in both radius and height in a disk (Drimmel & Spergel 2001), the extinction along any disk sightline can be approximated as

$$A_{K_L} = \frac{1 - e^{-|D_L(\sin b)/h_{\text{dust}}|}}{1 - e^{-|D_S(\sin b)/h_{\text{dust}}|}} A_K \quad (13)$$

where h_{dust} is the dust scale height fixed at $h_{\text{dust}} = 0.10 \pm 0.02$ kpc and D_S is the distance to the source derived in Section 4. We use the A_K extinction value calculated as shown in Section 2. This gives us a value for the K -band lens extinction of $A_{K_L} = 0.179$.

In Figure 6 the isochrone constraint is in purple, the dashed lines indicate the error on the measured lens magnitude, the Einstein angular radius is shown in sea green, and the microlensing parallax constraint is in gray. The result of the combined mass and distance relations is in perfect agreement with the MCMC mean and rms results yielded by the light-curve model fit with the Keck (AO) constraints (Table 7) and shown in Figure 7 in magenta. We confirm that the host is an M dwarf and the planet has the mass of Saturn with a projected separation

$$r_{\perp} = sD_L\theta_E, \quad (14)$$

and we find $r_{\perp} = 3.140 \pm 0.281$ au.

Table 7
Lens Parameters Table

Parameters	Units	Values and 1σ
M_h	M_{\odot}	0.495 ± 0.054
M_p	M_{Jup}	0.260 ± 0.028
D_L	kpc	3.476 ± 0.357
r_{\perp}	au	3.140 ± 0.281
θ_E	mas	0.785 ± 0.017

6. Discussion

We observed OGLE-2013-BLG-0132 using AO techniques with Keck three months and 7.4 yr after the microlensing event. Our 2020 high angular resolution images showed a clear separation between source and lens. This is the sixth microlensing event where the relative positions and flux ratio between source and lens were accurately measured. We used an MCMC routine of the DAOPHOT package (Terry et al. 2021) and a jackknife routine of KAI as in Bhattacharya et al. (2021), and deduced the flux of the lens and a ten times more accurate value for the Einstein angular radius. Our analysis has showed a separation of 56.91 ± 0.29 mas, which yields $\mu_{\text{rel, helio}} = 7.695 \pm 0.039$ mas yr $^{-1}$. We confirm the results presented by Mróz et al. (2017) for the microlensing event OGLE-2013-BLG-0132, then refine them.

As a consequence of the high precision of our AO results we were able to use a modified version of the Bennett & Rhie (1996) and Bennett (2010) process. We fit the event’s light curve while constraining the best-fit model using the Einstein angular radius, relative proper motion, and source flux in the K band that we deduce from the high angular resolution image analysis. This is the most rigorous way to find light-curve parameters able to define the source and lens system without inconsistencies. Using the AO follow-up constraints we

OGLE-2013-BLG-0132 Properties with Keck Constraint

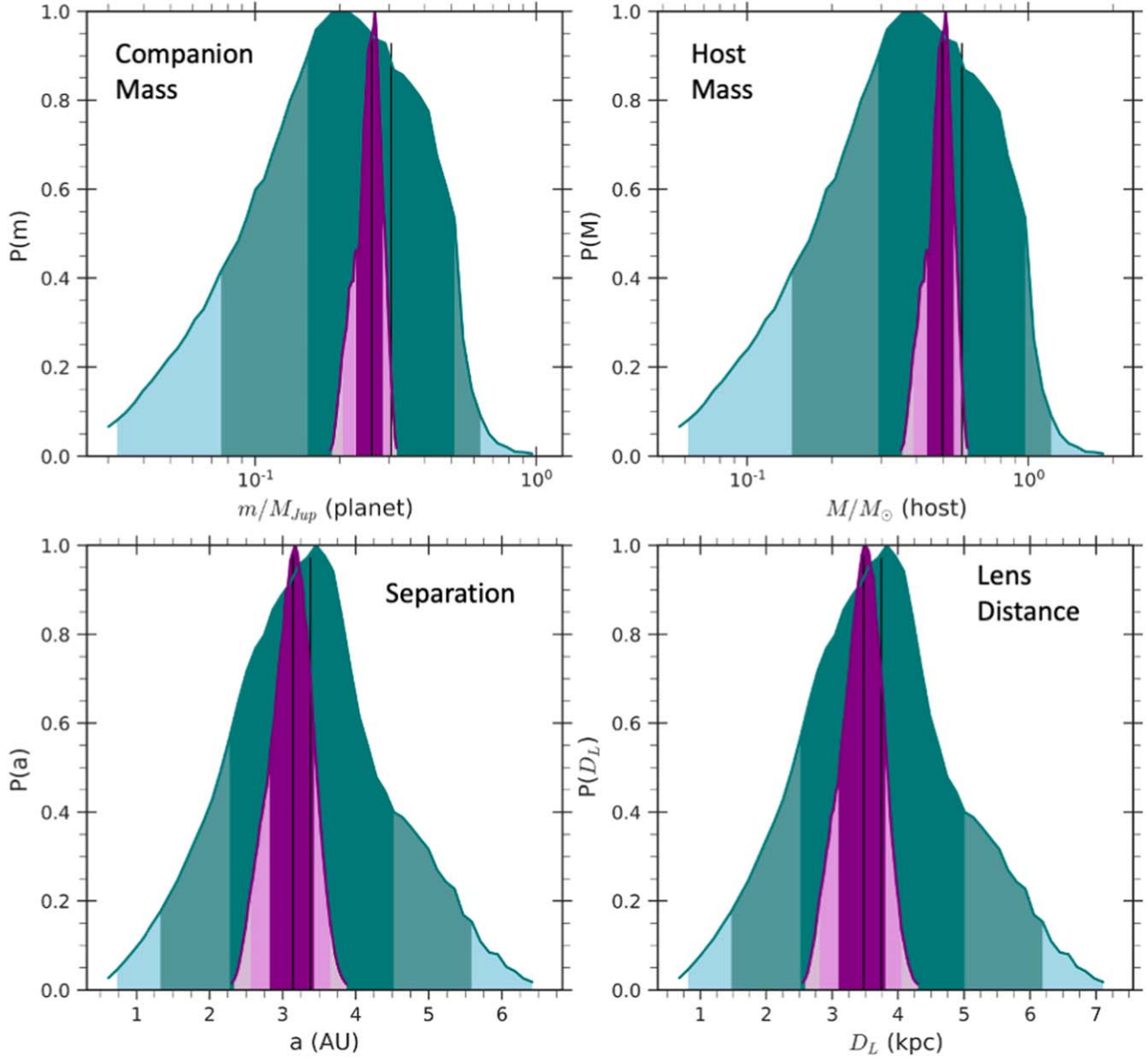


Figure 7. Bayesian posterior probability distributions for the planetary companion mass, host mass, their separation, and the distance to the lens system are shown with only light-curve constraints in blue and with the additional constraints from our Keck follow-up observations in red. The central 68.3% (1σ) of the distributions are shaded in darker colors (dark magenta and dark cyan), and the remaining central 95.4% (3σ) of the distributions are shaded in lighter colors. The vertical black line marks the median of the Bayesian probability distribution for the respective parameters. We show that the medians of the Bayesian probability are within 2σ of the constrained parameter distributions.

successfully fit the microlensing parallax and the distance to the source. Our light-curve best-fit model is in agreement with the previous results. Our fitted microlensing parallax is in agreement with the predicted values from the Galactic model (Koshimoto et al. 2021). Our measurement of the finite-source effects and the mass and distance of the planetary system validate the estimates predicted in Mróz et al. (2017).

We find the source angular radius to be $\theta_* = 0.80 \pm 0.08 \mu\text{as}$, at a distance of 7.405 kpc, which means that the source star must have a radius of $\sim 1.27 R_\odot$. We also measured the source brightness in the K band to be $K_{S,0} = 17.32 \pm 0.04$. This makes the source star a possible early G or late F-type star placed in the Galactic bulge. Finally, our measurements

confirm that the OGLE-2013-BLG-0132 event consists of an M dwarf host star with mass $M_h = 0.495 \pm 0.054 M_\odot$ and a Saturn-mass planet with $M_p = 0.26 \pm 0.028 M_{\text{Jup}}$ orbiting beyond the location of the snow line (2.7 au) at 3.14 ± 0.28 au. With a mass ratio of $q = 5 \times 10^{-4}$ this system is placed just outside the planet desert ($1 \times 10^{-4} < q < 4 \times 10^{-4}$) predicted by the core accretion theory (Ida & Lin 2004) and by the existing population synthesis models (Laughlin et al. 2004; Mordasini et al. 2009).

However, most of these theoretical work consider the planet and host star masses instead of mass ratios. As mentioned in Section 1, Ida & Lin (2004) predict the planetary desert for masses between 10 and $100 M_\oplus$, explaining that planets'

masses grow rapidly from 10 to 100 M_{\oplus} ; the gas giant planets rarely form with asymptotic masses in this intermediate range. Figure 7 of Suzuki et al. (2016) indicates that the detection efficiency for planets like OGLE-2005-BLG-071Lb (Bennett et al. 2020) and MOA-2008-BLG-379Lb (Bennett et al. 2023) of $\simeq 6 \times 10^{-3}$ or 7×10^{-3} is about five times larger than the detection efficiency for planets with $q \simeq 5 \times 10^{-4}$, like OGLE-2013-BLG-0132 and OGLE-2006-BLG-109Lc (Gaudi et al. 2008; Bennett et al. 2010). Our results in addition to these other similar results presented in Section 1 tend to agree with the conclusion of Suzuki et al. (2016) that sub-Saturn-mass planets are likely to be five times more common than super-Jupiters for early M dwarfs instead of just the average over all planets detectable by microlensing. This is a step toward understanding the dependence of the exoplanet mass ratio function on host mass.

Creating a large sample of low host star masses and their companions is of crucial importance for studies of occurrence rate measurements (Pass et al. 2023) and for population synthesis models, as it provides a more complete exploration of the parameter space of the observational detection bias used (Emsenhuber et al. 2023). The high sensitivity of gravitational microlensing to detect companion planets to this type of star, in combination with high angular resolution follow-up observations promises a large number of high-precision planet detections with the Nancy Grace Roman Space Telescope.

Another notable point we infer from this work is that OGLE-2013-BLG-0132 is a perfect candidate for Hubble Space Telescope follow-up observations. The results of the different observations and analysis methods of this study are in absolute agreement between them with very high precision. This makes this event an excellent candidate to test and ameliorate our techniques of measuring the planet and host star masses with/for the Nancy Grace Roman Space Telescope. Our Keck images show a clear separation between source and lens; observations in different bands with the Hubble Space Telescope will help us better acquire the systematic error sources in our methods. Finally, measuring the microlensing parallax for events of short length can be difficult, even by processing different observational bands, which makes this target even more interesting for testing and validating the parallax measurement methods.

Acknowledgments


N.E.R. would like to acknowledge Mr. Ioannis Vartholomeos for his precious help during this work, by providing interesting discussions and fruitful questions about the gravitational microlensing technique. Unfortunately, Mr. Vartholomeos passed away on 2023 June and did not have the chance to see this work completed.

This work was supported by the University of Tasmania through the UTAS Foundation and the endowed Warren Chair in Astronomy and the ANR COLD-WORLDS (ANR-18-CE31-0002) and by NASA through grant NASA-80NSSC18K0274. This research was also supported by the Australian Government through the Australian Research Council Discovery Program (project number 200101909) grant awarded to A.C. and J.P.B. The Keck Telescope observations and analysis were supported by a NASA Keck PI Data Award, administered by the NASA Exoplanet Science Institute. Data presented herein were obtained at the W. M. Keck Observatory from telescope time allocated to the National Aeronautics and

Space Administration through the agency's scientific partnership with the California Institute of Technology and the University of California. The Observatory was made possible by the generous financial support of the W. M. Keck Foundation. The authors wish to recognize and acknowledge the very significant cultural role and reverence that the summit of Maunakea has always had within the indigenous Hawaiian community. We are most fortunate to have the opportunity to conduct observations from this mountain.

ORCID iDs

Natalia E. Rektsini  <https://orcid.org/0000-0002-1530-4870>

Clément Ranc  <https://orcid.org/0000-0003-2388-4534>

Jean-Philippe Beaulieu  <https://orcid.org/0000-0003-0014-3354>

Joshua W. Blackman  <https://orcid.org/0000-0001-5860-1157>

Andrew A. Cole  <https://orcid.org/0000-0003-0303-3855>

Sean K. Terry  <https://orcid.org/0000-0002-5029-3257>

Naoki Koshimoto  <https://orcid.org/0000-0003-2302-9562>

Jean-Baptiste Marquette  <https://orcid.org/0000-0002-7901-7213>

References

- Batista, V., Beaulieu, J. P., Bennett, D. P., et al. 2015, *ApJ*, 808, 170
 Beaulieu, J.-P., Batista, V., Bennett, D., et al. 2018, *AJ*, 155, 78
 Beaulieu, J.-P., Bennett, D., Batista, V., et al. 2016, *ApJ*, 824, 83
 Bennett, D., Rhie, S., Udalski, A., et al. 2016, *AJ*, 152, 125
 Bennett, D., Udalski, A., Han, C., et al. 2018, *AJ*, 155, 141
 Bennett, D. P. 2014, *BAAS*, 46, 008
 Bennett, D. P., Bhattacharya, A., Anderson, J., et al. 2015, *ApJ*, 808, 169
 Bennett, D. P., Bhattacharya, A., Beaulieu, J.-P., et al. 2020, *AJ*, 159, 68
 Bennett, D. P., Bhattacharya, A., Beaulieu, J.-P., et al. 2023, arXiv:2311.00627
 Bennett, D. P., & Khavinson, D. 2014, *PhT*, 67, 64
 Bennett, D. P., & Rhie, S. H. 1996, *ApJ*, 472, 660
 Bennett, D. P., Rhie, S. H., Nikolaev, S., et al. 2010, *ApJ*, 713, 837
 Bennett, D. P. 2010, *ApJ*, 716, 1408
 Bensby, T., Adén, D., Melendez, J., et al. 2011, *A&A*, 533, A134
 Bertin, E., & Arnouts, S. 1996, *A&AS*, 117, 393
 Bertin, E. 2010, SWarp: Resampling and Co-adding FITS Images Together, Astrophysics Source Code Library, ascl:1010.068
 Bessell, M. S., & Brett, J. M. 1988, *PASP*, 100, 1134
 Bhattacharya, A., Beaulieu, J.-P., Bennett, D. P., et al. 2018, *AJ*, 156, 289
 Bhattacharya, A., Bennett, D. P., Beaulieu, J. P., et al. 2021, *AJ*, 162, 60
 Bhattacharya, A., Bennett, D. P., Beaulieu, J. P., et al. 2023, *AJ*, 165, 206
 Blackman, J. W., Beaulieu, J. P., Bennett, D. P., et al. 2021, *Natur*, 598, 272
 Bond, I., Abe, F., Dodd, R., et al. 2001, *MNRAS*, 327, 868
 Bond, I., Bennett, D., Sumi, T., et al. 2017, *MNRAS*, 469, 2434
 Bond, I. A., Udalski, A., Jaroszyński, M., et al. 2004, *ApJL*, 606, L155
 Boyajian, T. S., van Belle, G., & von Braun, K. 2014, *AJ*, 147, 47
 Burn, R., Schlecker, M., Mordasini, C., et al. 2021, *A&A*, 656, A72
 Dong, S., Gould, A., Udalski, A., et al. 2009, *ApJ*, 695, 970
 Drimmel, R., & Spergel, D. N. 2001, *ApJ*, 556, 181
 Emsenhuber, A., Mordasini, C., & Burn, R. 2023, *EPJ*, 138, 181
 Gaudi, B. S. 2012, *ARA&A*, 50, 411
 Gaudi, S., Bennett, D. P., Udalski, A., et al. 2008, *Sci*, 319, 927
 Girardi, L., Bertelli, G., Bressan, A., et al. 2002, *A&A*, 391, 195
 Gould, A. 2008, *ApJ*, 681, 1593
 Ida, S., & Lin, D. N. C. 2004, *ApJ*, 616, 567
 Kennedy, G. M., & Kenyon, S. J. 2008, *ApJ*, 673, 502
 Koshimoto, N., Baba, J., & Bennett, D. P. 2021, *ApJ*, 917, 78
 Koshimoto, N., & Ranc, C. 2022, nkoshimoto/genulens: Release v1.2, Zenodo, doi:10.5281/ZENODO.6869520
 Koshimoto, N., Udalski, A., Beaulieu, J. P., et al. 2016, *AJ*, 153, 1
 Kraft, D. 1985, in *Computational Mathematical Programming*, ed. K. Schittkowski (Berlin: Springer), 261
 Laughlin, G., Bodenheimer, P., & Adams, F. C. 2004, *ApJL*, 612, L73

- Lissauer, J. J. 1993, *ARA&A*, 31, 129
- Lu, J. R., Gautam, A. K., Chu, D., Terry, S. K., & Do, T. 2021, *Keck-DataReductionPipelines/KAI: v1.0.0 Release of KAI*, Zenodo, doi:10.5281/ZENODO.6677744
- Minniti, D., Lucas, P., Emerson, J., et al. 2010, *NewA*, 15, 433
- Miyake, N., Sumi, T., Dong, S., et al. 2011, *ApJ*, 728, 120
- Mordasini, C., Alibert, Y., & Benz, W. 2009, *A&A*, 501, 1139
- Mróz, P., Udalski, A., Bond, I. A., et al. 2017, *AJ*, 154, 205
- Nataf, D. M., Gould, A., Fouqué, P., et al. 2013, *ApJ*, 769, 88
- Nishiyama, S., Tamura, M., Hatano, H., et al. 2009, *ApJ*, 696, 1407
- Pass, E. K., Winters, J. G., Charbonneau, D., et al. 2023, *AJ*, 166, 11
- Pollack, J. B., Hubickyj, O., Bodenheimer, P., et al. 1996, *Icar*, 124, 62
- Ranc, C. 2020, *Microlensing Observations ANALysis tools*, v0.1, Zenodo, doi:10.5281/zenodo.4257009
- Ranc, C., Cassan, A., Albrow, M. D., et al. 2015, *A&A*, 580, A125
- Schneider, P., & Weiss, A. 1986, *A&A*, 164, 237
- Shopbell, P., Britton, M., & Ebert, R. 2005, in *ASP Conf. Ser. 347, Astronomical Data Analysis Software and Systems XIV* (San Francisco, CA: ASP)
- Stetson, P. B. 1987, *PASP*, 99, 191
- Surot, F., Valenti, E., Gonzalez, O., et al. 2020, *A&A*, 644, A140
- Suzuki, D., Bennett, D. P., Sumi, T., et al. 2016, *ApJ*, 833, 145
- Suzuki, D., Bennett, D. P., Udalski, A., et al. 2018, *AJ*, 155, 263
- Suzuki, D., Udalski, A., Sumi, T., et al. 2013, *ApJ*, 780, 123
- Terry, S. K., Bhattacharya, A., Bennett, D. P., et al. 2021, *AJ*, 161, 54
- Tukey, J. 1958, *Ann. Math. Stat.*, 29, 614
- Udalski, A., Jaroszyński, M., Paczyński, B., et al. 2005, *ApJL*, 628, L109
- Udalski, A., Szymanski, M., Mao, S., et al. 1994, *ApJ*, 436, L103
- Udalski, A., Szymanski, M. K., Kubiak, M., et al. 2004, arXiv:astro-ph/0411543
- Vandorou, A., Bennett, D. P., Beaulieu, J.-P., et al. 2020, *AJ*, 160, 121
- Vandorou, A., Dang, L., Bennett, D. P., et al. 2023, arXiv:2302.01168
- Winters, J. G., Henry, T. J., Lurie, J. C., et al. 2015, *AJ*, 149, 5